APPLIED SCIENCES AND ENGINEERING

A programmable and skin temperature–activated electromechanical synergistic dressing for effective wound healing

Guang Yao[1,2,3]*, Xiaoyi Mo[1], Chenhui Yin[1], Wenhao Lou[1], Qian Wang[1], Sirong Huang[1], Linna Mao[1], Sihong Chen[1], Kangning Zhao[4], Taisong Pan[1,2,3], Lin Huang[5]*, Yuan Lin[1,2,3]*

Mechanical regulation and electric stimulation hold great promise in skin tissue engineering for manipulating wound healing. However, the complexity of equipment operation and stimulation implementation remains an ongoing challenge in clinical applications. Here, we propose a programmable and skin temperature–activated electromechanical synergistic wound dressing composed of a shape memory alloy-based mechanical metamaterial for wound contraction and an antibacterial electret thin film for electric field generation. This strategy is successfully demonstrated on rats to achieve effective wound healing in as short as 4 and 8 days for linear and circular wounds, respectively, with a statistically significant over 50% improvement in wound closure rate versus the blank control group. The optimally designed electromechanical synergistic stimulation could regulate the wound microenvironment to accelerate healing metabolism, promote wound closure, and inhibit infection. This work provided an effective wound healing strategy in the context of a programmable temperature-responsive, battery-free electromechanical synergistic biomedical device.

INTRODUCTION

Skin wound management, especially for wounds with diminished healing ability caused by extreme external injuries or chronic illnesses, represents a central concern in clinical care and remains a notable problem in public health (*1*, *2*). According to a recent global survey by the World Health Organization, acute or chronic wound problems plague over 305 million people worldwide (*3*). Chronic wound management results in long-term physical and mental suffering because of the protracted treatment courses and a rapidly growing global economic burden. For example, more than 25 billion dollars is spent annually on wound management in the United States alone, and projected worldwide expenditure would reach 80 billion dollars by 2024 (*4*, *5*). With the tremendous advancements of modern biomedical technology, numerous potential pharmacological or nonpharmacological therapies have been developed to manipulate the wound repair process (*6*, *7*). Nevertheless, most drugs can either exert an insignificant effect on wound healing or induce severe side effects such as allergies and nausea (*8*). The cell-based strategies such as growth factor–mediated therapy emerged as a promising approach for promoting skin wound healing (*9*, *10*), which is still in the preclinical stage and faces the challenges of being easily contaminated, inactivated, and degraded. Nonpharmacological physical therapies, including mechanical regulation, electrostimulation, ultrasound, etc., have been approved by the U.S. Food and Drug Administration (FDA) and recognized as effective approaches with biosafety for damage repair and tissue regeneration (*6*, *11*–*14*). These noninvasive approaches have the potential to manipulate the biological microenvironment to control endogenous cell behaviors, activate cell-related gene expression, promote the proliferation and differentiation of tissue cells, and actively stimulate tissue regeneration (*15*–*17*). However, clinically available nonpharmacological stimulations rely on large-sized extracorporeal equipment, primarily limited by professional equipment operation and complex implementation (*18*, *19*). Therefore, noninvasive, efficient, cost-effective, and convenient approaches are always desired for treating skin wounds.

Wound dressings have been extensively used to treat skin wounds since they have the advantages of easy use, reducing the risk of infection, and painless removal (*20*). To further promote wound healing, most existing strategies of wound dressings mainly focus on the biochemical functions such as delivery and trigger of biologically active agents (*21*). Still, they are often associated with the high cost and complex processes of the loading and controlled activation of the bioactive agents. Recently, to achieve rapid wound closure, the principal goal of skin wound management, sophisticated nonpharmacological wound dressings providing electrostimulation or mechanical regulation have been delicately developed and demonstrated outstanding effectiveness (*22*, *23*). The efficient wound closure effect of the electrostimulation can be attributed to electric field–facilitated relevant cell migration, proliferation, and differentiation for promoting wound healing metabolism (*24*). On the other hand, mechanical regulation can generate contractile strains to enhance vascularization for nutritional supply, lower scar volume, and avoid keloid incidence (*25*–*27*). However, the reported discrete electrostimulation based on piezoelectric and triboelectric wearable devices must be driven by the regular or irregular spontaneous motions of organisms (*28*, *29*), limiting the healing effect of the wound site without experiencing frequent activities. Electrical intervention

[1]School of Materials and Energy, University of Electronic Science and Technology of China, Chengdu 610054, Sichuan, China. [2]State Key Laboratory of Electronic Thin films and Integrated Devices, University of Electronic Science and Technology of China, Chengdu 610054, Sichuan, China. [3]Medico-Engineering Cooperation on Applied Medicine Research Center, University of Electronic Science and Technology of China, Chengdu 610054, Sichuan, China. [4]State Key Laboratory of Advanced Technology for Materials Synthesis and Processing, International School of Materials Science and Engineering, Wuhan University of Technology, Wuhan 430070, Hubei, China. [5]School of Electronic Science and Engineering, the Center for Information in Medicine, University of Electronic Science and Technology of China, Chengdu 611731, Sichuan, China.
*Corresponding author. Email: gyao@uestc.edu.cn (G.Y.); lhuang@uestc.edu.cn (L.H.); linyuan@uestc.edu.cn (Y.L.)

based on electrets has been applied for wound healing and fracture repair, and the voltage decay of the external static electric field limits the long-term operation (*30*, *31*). In addition, mechanical contraction regulation can inhibit or promote vascularization depending on the strain magnitudes. A recent in vitro study also revealed that extracellular matrix has a positive significant overall effect in vascularization at ~10% strain during tissue regeneration (*32*). As a generic physical technology, negative pressure wound therapy (NPWT) has become widely adopted for a broad range of treatment goals. For wound treatment, the NPWT is recommended to be used within an effective therapeutic pressure range of −50 to −150 mmHg (*33*, *34*). However, how to generate a suitable contraction force based on a minor strain is an urgent problem. Simultaneously, there was very little in-depth research to address personalized customization to manipulate orderly healing of different-shaped wounds. Thus, combining the effect of electrostimulation and mechanical contraction regulation, avoiding their limitations by designing new electromechanical synergistic dressings (EMSDs) so as to accelerate wound healing more effectively has been a pressing issue.

Here, we present a flexible and seamlessly attachable EMSD, which consists of a shape memory alloy (SMA)–based mechanical metamaterial grid and an antibacterial electret electrostatic thin film (EEF) for applying electromechanical synergistic stimulations to effectively promote wound healing. Biocompatible SMAs have been authorized for biomedical applications by FDA, which can be triggered to provide a sufficient actuation force with a minor strain for drawing the epithelial tissues (*35*, *36*). According to linear or circular wounds, the SMA metamaterial grid can be programmed to render appropriate contraction force based on a minor contractile strain (~10%). The patterned antibacterial EEF can promote the healing process by strengthening the endogenous electric field. In vivo studies on rats under the EMSD treatment showed significantly accelerated wound healing in as short as 4 and 8 days for linear and circular wounds, respectively. Compared to the blank controls, the wound closure rate of the EMSD stimulation group was improved by more than 50%, superior to most current nonpharmacological physical stimulation approaches. Mechanism study revealed that the electromechanical synergistic stimulation could enhance the secretion of relevant typical growth factors including epidermal growth factor (EGF), transforming growth factor–β (TGF-β), and vascular endothelial growth factor (VEGF), to regulate wound microenvironment for promoting healing metabolism and wound closure. This work provided a programmable, battery-free, and skin temperature–activated electromechanical synergistic therapy for effective wound treatment.

RESULTS

Working principle and characterization of the EMSD

The EMSDs applied for linear and circular wound healing were defined as EMSD for linear wounds (EMSD-L) and circular wounds (EMSD-C), respectively. As shown in Fig. 1A, the flexible sandwich-structured EMSD consists of four layers: an SMA metamaterial layer triggered by skin temperature to provide mechanical contraction force, a polarized polytetrafluoroethylene (PTFE) EEF generating an electrostatic electric field, and two flexible Ecoflex encapsulation layers to fit the nonplanar skin surface seamlessly. The detailed fabrication procedure of EMSDs is included in fig. S1. The SMA metamaterials and EEF can be designed to render contraction and external electric fields according to a linear or circular wound. Mounting together, the programmable EMSDs were prepared to accelerate wound healing (Fig. 1B). The EMSD-L comprises an anisotropic metamaterial grid and a rectangular EEF (a rectangular negative electrode and a rectangular ring positive electrode), while the EMSD-C consisted of an isotropic metamaterial grid and a circular EEF (a circular negative electrode and a circular ring positive electrode). The EMSD-L only achieves the uniaxial stretching property because of its mechanical designs, while the EMSD-C can be biaxially stretched in vertical and horizontal directions. The overall dimensions of the EMSD-L and EMSD-C in their initial state are approximately $37 \times 27 \times 0.2$ mm^3 and $28 \times 28 \times 0.2$ mm^3, respectively (Fig. 1C, left). In addition, the EMSDs could be subjected to very large deformation, such as being twisted multiple turns (Fig. 1C, middle). Skin temperature can trigger the stretched and twisted EMSDs to restore the initial state and ensure contraction force on linear or circular skin wounds (movies S1 and S2). Figure 1C (right) showed the experimental setup for EMSD-driven linear and circular incisional wound healing. A three-dimensional microscope was used to examine the uniformity and height information of the multilayered components. The top- and the side-view scanned images are shown in Fig. 1D. The cross-sectional height profile taken along one scanning line further quantified the multilayered geometry. The overall thickness of the EMSD is ~217 μm, and the thickness of the PTFE electret film, the SMA grid, and the Ecoflex encapsulation layer are 59, 93, and 65 μm, respectively (Fig. 1E). To confirm the biocompatibility of the packaged EMSD, mouse fibroblasts were cultured on the encapsulated device surface and in a reference cultural dish for 3 days to examine and compare the cell attachment, proliferation, and morphology. Cells in both media exhibited similar density and equivalent morphology, and the fluorescence staining results showed that the cells could spread and form intact cytoarchitecture in both groups (Fig. 1F). In addition, the relative viability of cells on encapsulation material was more than 98% within 3 days, comparable to the cells cultured in the culture dish (Fig. 1G). These results confirmed that the encapsulated EMSD is noncytotoxic and biocompatible.

Design and performance of the SMA metamaterial grids

The designs of the SMA metamaterial gird for the linear wound (SMA-L) and the circular wound (SMA-C) rely on network construction in a periodic lattice topology (*37*–*39*). The unicellular building blocks, partially enlarged block elements (pink dotted frames), and various designs of the SMA-L and SMA-C are illustrated in Fig. 2 (A to D). For the twofold symmetric SMA-L, the unicellular bottom length, the distance between the middle corner, and the thickness of the unicellular wall are 1.8, 0.6, and 0.18 mm, respectively. The adjustable angle between the bevel and bottom and the bevel length are defined as α and l, respectively. The l is determined by the cosine relationship of α, the distance between the middle corner, and the unicellular bottom length (Fig. 2A). The relationship between the unicellular parameters and the nondimensional Young's modulus of the grid with similar configuration has been reported in previous works (*40*), and the nondimensional Young's modulus along the x axis and y axis was defined as E_x/E_{SMA} and E_y/E_{SMA}, respectively. As the α increases in the range of 5° to 85°, the E_x/E_{SMA} decreases and the E_y/E_{SMA} increases monotonously, respectively (fig. S2 and note S1). In addition, finite element analysis (FEA) results show that α = 50° is the critical point of the elastic

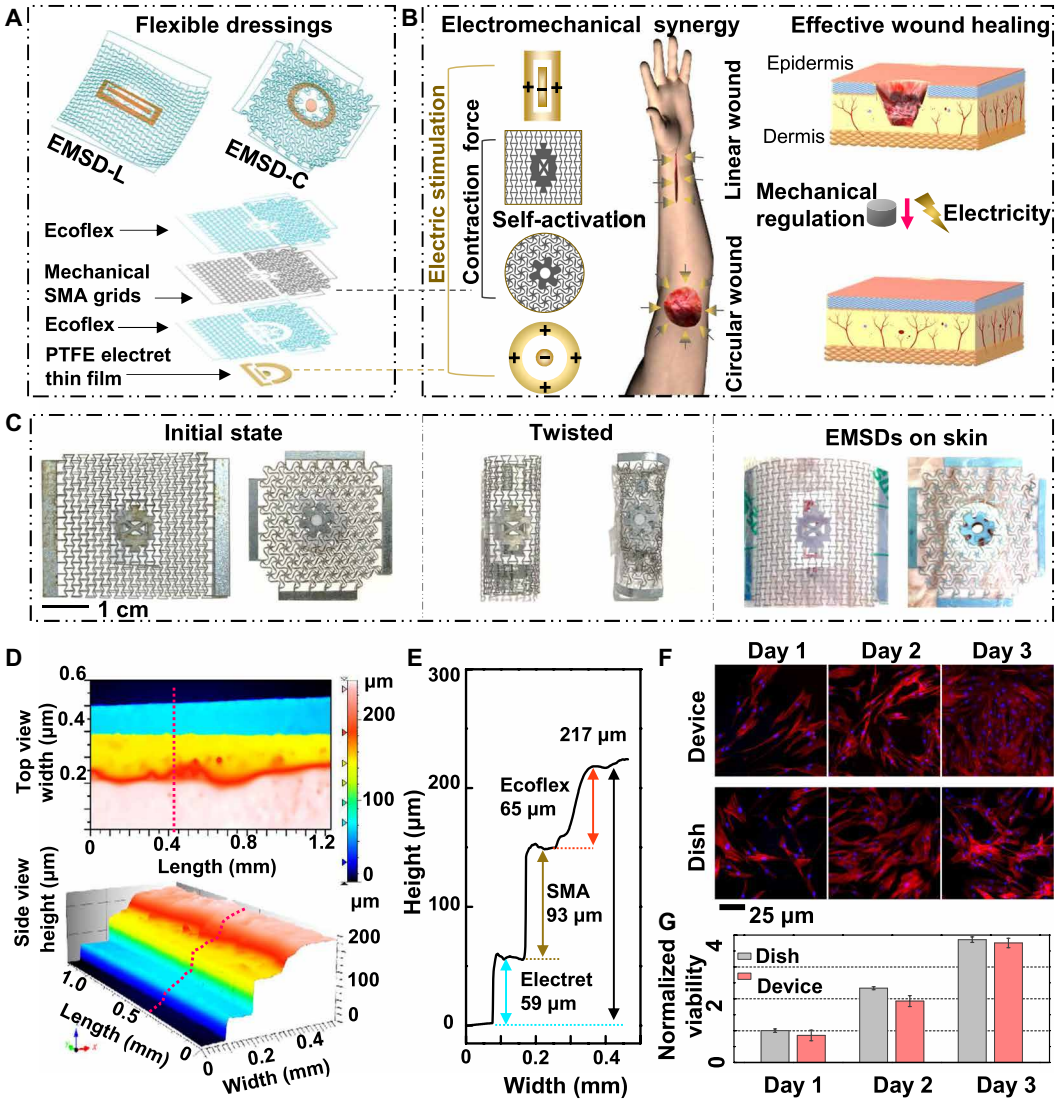

Fig. 1. Working principle and characterization of the EMSD. (**A**) Schematics of the overall EMSD-L and EMSD-C (top). Exploded illustration of the device components, essential materials, and multilayer structures (bottom). (**B**) Working principle of wound treatment by programmable and skin temperature–activated EMSDs. (**C**) Optical images of the initial state (left), twisted state (middle), and experimental setup for wound treatment (right) of the EMSDs. (**D**) Top- and side-view three-dimensional microscope images of the multilayer structures. (**E**) Height profile along the pink line in (D) showing the height of multilayer components. (**F**) Fluorescence images of stained fibroblasts cultured on a regular cell culture dish and the Ecoflex. (**G**) Comparison of normalized cell viability for 3 days showing excellent biocompatibility of the packaged device. All data in (G) are presented as means ± SD.

strain threshold (8%) when the tensile strain is 10% (fig. S3). Because the E_x/E_{SMA} decreases monotonously as the α increases, considering the suitable stretchability and contraction force, the α of the SMA-L was designed to be 50°, 60°, and 70°, and the corresponding l is 0.93, 1.2, and 1.75 mm (Fig. 2B). As shown in Fig. 2C, for the sixfold rotationally symmetric SMA-C, the unicellular construction exploits a triangular lattice pattern, and one side of the triangle consists of two arcs and three straight lines, where the two straight lines at the port serve as the common part of the two-block elements to connect lattice nodes. The width and radius of the arc are 0.12 and 0.41 mm, and the width and length of the straight line are 0.24 and 1.18 mm, respectively. The arc angle as the only variable is defined as β. Researchers have reported the relationship between the unicellular parameters and the grid's nondimensional Young's modulus. As the β increases in the range of 90° to 180°, the E/E_{SMA} of the SMA-C decreases monotonously, and the 120° grid has the most significant stress in the elastic strain region under 10% tensile strain (*41*). In this experiment, the β was designed to be 110°, 120°, and 130°, respectively (Fig. 2D, fig. S4, and note S1).

FEA and experimental results of the SMA metamaterial grids under a series of tensile distances are shown in Fig. 2E and fig. S5. FEA results of the metamaterial grids under 0 and 10% tensile deformation (the 60° SMA-L was stretched 4 mm along the x axis, and the 120° SMA-C was biaxially stretched 3 mm) demonstrated that the strain was evenly distributed on the unicellular building blocks. Commercial uniaxial and biaxial tensile systems were then used to test the corresponding experimental mechanical response of the stretchable SMA-L and SMA-C, respectively. Similar deformation

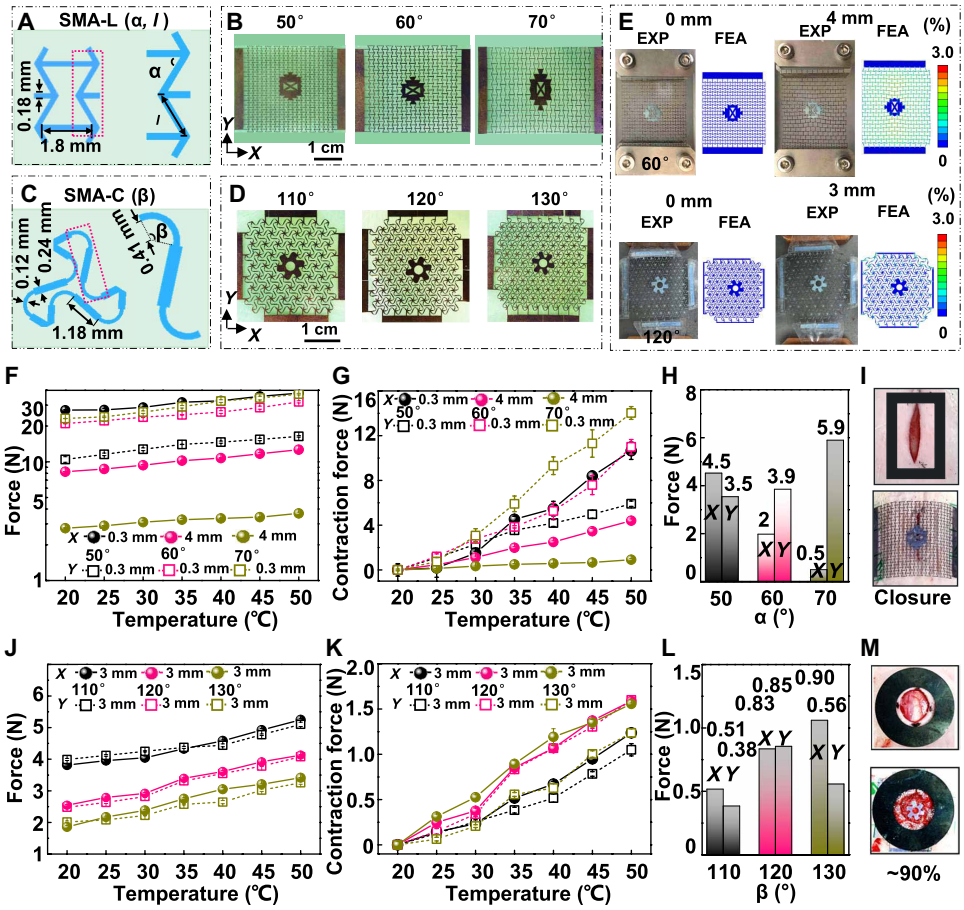

Fig. 2. Design and performance of the SMA metamaterial grids. (**A**) Schematic illustrations of the unit cell and partially enlarged block elements of the SMA-L. (**B**) Optical images of SMA-L with different α. (**C**) Schematic drawings of the unit cell and partially enlarged block elements of the SMA-C. (**D**) Optical images of SMA-C with different β. (**E**) Experimental (EXP) and FEA results for the SMA-L and SMA-C at 0 and 10% strain. (**F**) The uniaxial tensile force of SMA-L in the temperature range of 20° to 50°C with intervals of 5°C. (**G**) The contraction force of the SMA-L extracted from (F). (**H**) The SMA-L contraction force at 35°C. (**I**) A 60° SMA-L was chosen for the linear wound treatment. (**J**) The biaxial tensile force of SMA-C in the temperature range of 20° to 50°C with intervals of 5°C. (**K**) The contraction force of the SMA-C extracted from (J). (**L**) The SMA-C contraction force at 35°C. (**M**) The circular wound area was reduced to 90% when the 120° SMA-C was used. All data in (F), (G), (J), and (K) are presented as means ± SD, and the round symbol and the square symbol in Fig. 2 (F, G, J, and K) represent the *x* axis and *y* axis data, respectively.

behaviors were observed in FEA and experimental results. The strain (3%) subjected by the mechanical grid was consistently smaller than the failure strain (8%) when the SMA metamaterial grids were stretched up to 10% deformation, showing their good stretchability within the designed deformation range. Then, the uniaxial stretching force of various designed SMA-L was tested under different ambient temperatures (20°, 25°, 30°, 35°, 40°, 45°, and 50°C) with a loading rate of 0.02 mm/s (Fig. 2F). The unicellular construction of the twofold symmetric nature renders an anisotropic property, which means that the SMA-L can be uniaxially stretched along the *x* axis. For the 50°, 60°, and 70° SMA-L, the *x* axis–stretching distances were 0.3, 4, and 4 mm, while the *y* axis–stretching distances were 0.3, 0.3, and 0.3 mm. The SMA-L cannot be stretched in both the *x* axis and *y* axis directions when α is 50° owing to its design characteristics (figs. S2 and S6). The stretched force increased as the ambient temperature rises because of the temperature response characteristics of the SMA. The contraction forces were calculated by the difference between the force value at 20°C and these values at different temperatures (Fig. 2G). The sharp increase (30° to 35°C) can be attributed to the phase transformation of the SMA (*42*, *43*). A_s is the temperature at which the phase transition begins, and A_f is the temperature at which the phase transition ends. In this experiment, the A_s and A_f of the NiTi-based SMA are about 24° and 33°C, respectively. The contraction force data at 35°C (~skin temperature) extracted from Fig. 2G are shown in Fig. 2H, which are 4.5, 2, and 0.5 N (*x* axis) and 3.5, 3.9, and 5.9 N (*y* axis) for the SMA-L of 50°, 60°, and 70°, respectively. As α increases, the *x* axis deformation resistance decreases, and the *y* axis deformation resistance increases, coinciding with the previously reported results (*40*). Simultaneously, the SMA-L is easy to stretch and retract in the *x* axis direction but has a prodigious equivalent elastic modulus in the *y* axis direction (fig. S2). This unconventional performance ensures the contraction and closure of the linear wound while avoiding unnecessary force along the incision direction to delay wound healing. Considering the suitable stretchability and contraction force, a 60° SMA-L was chosen for the linear wound contraction (Fig. 2I). For comparison, The SMA-C has similar biaxial tensile response properties in both the *x* axis and *y* axis, which can be attributed to the sixfold rotationally symmetric structure (Fig. 2, J and K). The contraction force extracted from Fig. 2K at 35°C of 110°, 120°, 130° are 0.51, 0.83, and 0.9 N

(*x* axis) and 0.38, 0.85, and 0.56 N (*y* axis) (Fig. 2L). Considering the similar biaxial contraction force, a 120° SMA-C was chosen for further animal studies. The wound area (0.8 cm in diameter) was reduced to around 90% when the SMA-C was used (Fig. 2M). Fracture limits of the SMA were tested to evaluate the feasibility of the practical application (fig. S7). The fracture limits are 14, 37, and 61.5% for 50°, 60°, and 70° SMA-L, respectively, and the fracture limits are 14, 17.3, and 18% for 110°, 120°, and 130° SMA-C, respectively. For both grids, the fracture limit increases monotonically during tensile deformation as the angle increases. Then, the EMSDs were worn on a human arm to simulate application scenarios, which can fit the skin surface and be worn stably and twisted (fig. S8). In addition, the actual application scenario of the EMSDs is a three-dimensional curved surface, and the average radius of the intervention site is approximately equal to 5 cm. On the basis of the calculation and FEA simulation results, the difference in contraction mechanism on the three-dimensional and flat surfaces is slight (fig. S9).

Design and performance of the EEF

Endogenous wound electric fields, induced when the epithelial layer is damaged and the transepithelial potential is disrupted, can promote epithelial cells to initiate directional migration for reepithelialization. Applying external electric fields in the default direction of wound healing have been recognized as a promising approach to strengthening endogenous electric fields and increasing the healing rate (*33*, *34*) (Fig. 3A). In contrast, applying reversed EF direction against the default wound healing direction will not enhance wound healing or hinder normal wound healing behavior (fig. S10). Five configurations of EEF were prepared for the configuration optimization, and the EEF configuration with the positive electrode outside and negative electrode inside was chosen for further animal experiments (fig. S11 and note S2). Here, the patterned EEF was used as the source of the external electric field. The EEF for the linear wound was composed of a 10 mm by 2 mm rectangular negative electrode and a rectangular ring positive electrode. The outer and inner rectangle dimensions of the positive electrode are 15 mm by 10 mm and 11 mm by 4 mm, while the EEF for the circular wound (EEF-C) contained a circular negative electrode (Φ = 3 mm) and a circular ring positive electrode. The diameter and inner diameter of the positive electrode are 12 and 6 mm. Optical images of the linear and circular incisional wound and experimental setup for EEF-driven wound healing are shown in Fig. 3 (B and C), respectively. The negative EEF electrode (−1 kV) was directly placed above the wound, and the positive EEF electrode (+1 kV) was placed to surround the damage. This potential is maintained until the skin regeneration process is completed. To evaluate the effectiveness of electric field penetration, Ansys Maxwell finite element solver (AMFES) was used to estimate the electric field strength at the wound site. AMFES simulation result showed that the patterned electrodes could generate a uniform electric field in its covered area (Fig. 3, D and E). The electric field rapidly attenuated within the first 2 mm into the skin and slowly decayed to a low value of ~0.2 V/cm at 10-mm depth inside epidermis and dermis (Fig. 3F), which is sufficient to increase the speed of epithelial migration into the wound (*44*, *45*). The AMFES simulation suggested that the EMSD implemented stable and effective electric field stimulations into the skin when applied to the wound area. In our design, the EEF electrodes were directly placed above

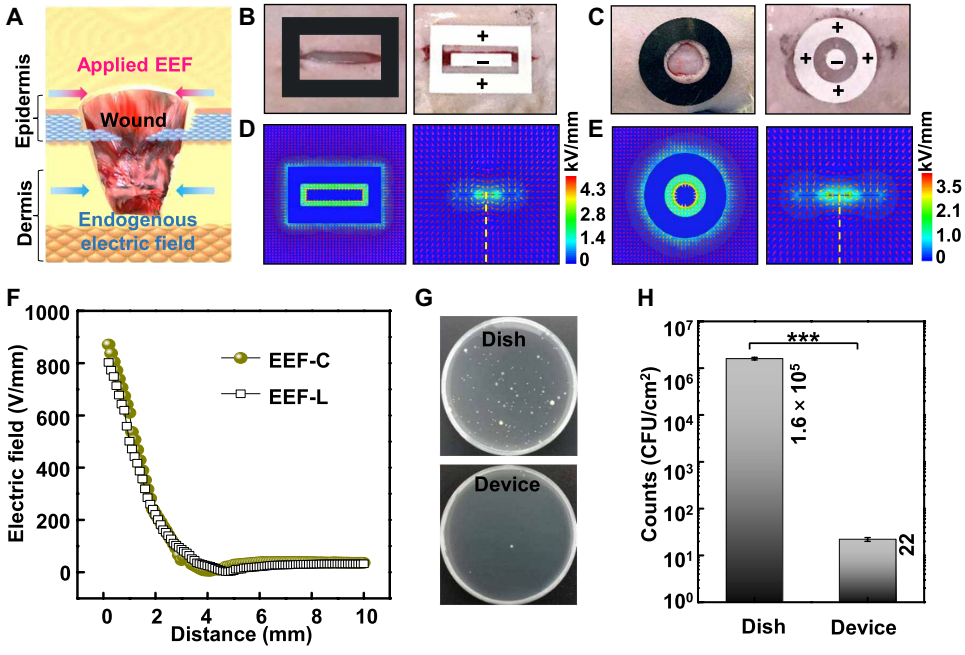

Fig. 3. Design and performance of the EEF. (**A**) Schematics of the external electric field to enhance the wound-induced endogenous electric field for effective wound healing. (**B**) Optical images of the linear incisional wound and experimental setup for EEF-driven healing. (**C**) Optical images of the circular incisional wound and experimental setup for EEF-driven healing. (**D**) AMFES simulated electric field distribution inside a linear wound. (**E**) AMFES simulated electric field distribution inside a circular wound. (**F**) AMFES simulated electric field strength as a function of the depth into the tissue extrapolated from (D) and (E). (**G**) Bacterial colony formation of *E. coli* on the EEF and an unpolarized PTFE film (control). (**H**) Antibacterial efficiencies under different conditions. All data in (H) are presented as means ± SD. CFU, colony-forming unit.

the wound to generate an electric field that could penetrate the dermis and to strengthen the endogenous electric field for enhanced wound healing. The antibacterial efficiency of the EEF was investigated by using *Escherichia coli* (ATCC 8739) as the model bacteria (*46*, *47*). The EEF was placed on the bottom in the first dish, and an unpolarized PTFE film was placed into another dish as the control. The *E. coli* stains initially containing bacteria (~7×10^3 colony-forming units/cm^2) were aerobically cultivated in two dishes at 37°C to the stationary phase with Luria-Bertani medium for 24 hours (Fig. 3G). The viable counts in the EEF dish and polyethylene film dish were 1.6×10^5 and 22, respectively (Fig. 3H), which indicated that the EEF has nearly 99.99% killing efficiency to *E. coli*. Thus, the electrostatic field induced by patterned EEF can promote the healing process by strengthening the endogenous electric field and inhibit infection through antibacterial function.

DISCUSSION

Wound healing by EMSD intervention and mechanism studies

As shown in Fig. 4A, the skin response to injury occurs in three overlapping cascade but distinct stages: the (i) inflammation stage, (ii) tissue formation stage, and (iii) remodeling stage (*6*). The inflammation stage occurs immediately after tissue damage to remove devitalized tissues and invade bacteria to prevent infection. The new tissue formation stage consists of related cellular proliferation and migration, new blood vessel and scab formation, and wound closure to restore the epithelium's barrier function. Last, the remodeling stage is characterized by the reorganization of disorganized collagen induced by migrated fibroblasts in the reepithelialized wound site. To study the influence of the as-prepared EMSD-L on the wound healing process, first, linear full-depth skin wounds (~1 cm long) on the nape and the dorsum of rats were created as the wound model (fig. S12). The linear wound healing performance was then investigated in four groups fed under the same conditions. As schematically displayed in Fig. 4B (left), the rats in the EMSD-L group were stimulated by an electromechanical synergistic device. Rats solely stimulated by SMA-based mechanical dressing (MD) and EEF-based electrical dressing (ED) for linear wound healing were divided into the MD-L and ED-L groups, respectively. In addition, the blank control (BC) group without a wearable device was defined as the BC-L group. All groups were subjected to the same linear wound surgery procedure, and the rats were labeled as EMSD-L_n, MD-L_n, ED-L_n, and BC-L_n (n = 1, 2, 3, 4). After surgery and before euthanasia, the wound healing process was documented once every 2 days, accompanied by replacing the EEF (Fig. 4B, right, fig. S13). This wound healing model was associated with only minor soft tissue trauma and a flexible dressing without affecting normal daily activity (movie S3). On day 0, with the linear wound model construction, the linear wound dehisced because of the loose skin of the rodent rats in the four groups. For the EMSD-L group, the linear wound started to close and a small amount of scab formed at the incision site on day 2, indicating that the healing process underwent the inflammation and tissue formation stages. On day 4, the gradual decrease in the wound line length and wound scab reflected the complete wound closure of the new tissue formation stage. The wound healing has entered the remodeling phase starting at day 6, marked by the blurring of the incision wound line. Similar wound healing processes were observed from the MD-L, ED-L, and BC-L groups, indicating that the EMSD did not alter the natural wound healing procedure. In both MD-L and ED-L groups, the scab began to form at day 2 and slowly evolved until day 4. However, during the entire 6-day monitoring period, the wound healing has been at the stages of inflammation and tissue formation since the wound line persisted and the scab was not eliminated. The skin at the linear incisional wound site in the different groups was collected at day 6 postintervention to further analyze the microscopic healing effect

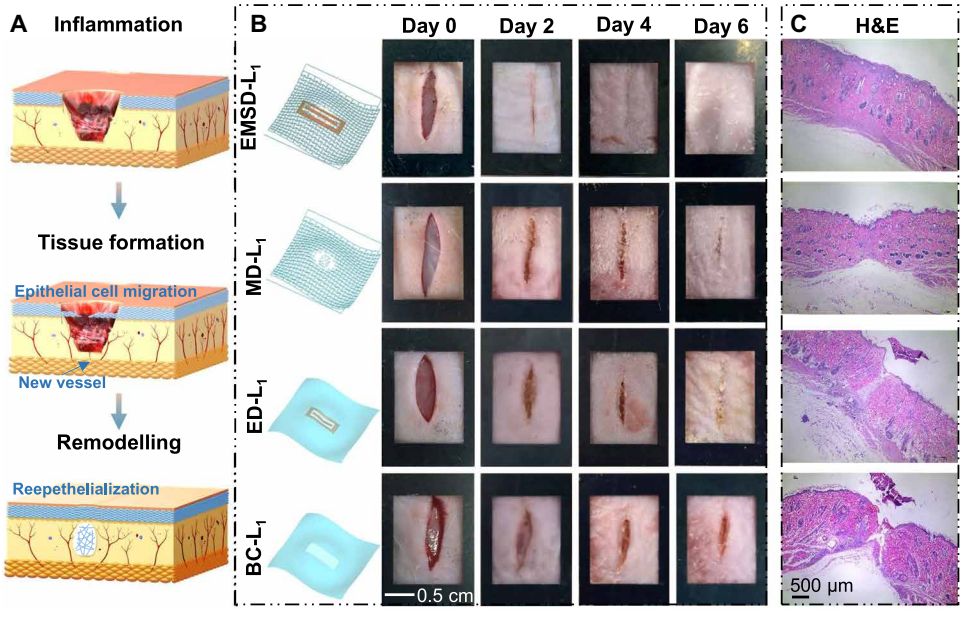

Fig. 4. Cascade stages of wound repair and linear incisional wound healing. (**A**) Three classic stages of wound healing: (i) inflammation, (ii) tissue formation, and (iii) remodeling. (**B**) A series of images on the wound area over time of the EMSD-L group, MD-L group, ED-L group, and BC-L group (F) (n = 4). Schematics on the left show the device setup of each group. (**C**) H&E stains of skin at the wound site.

by hematoxylin-eosin (H&E) staining (Fig. 4C). The wounds in the EMSD-L groups achieved reepithelialization formation and were in the remodeling phase, whereas the MD-L and ED-L groups exhibited granulation tissue at the wound site. In contrast, the epidermis was utterly absent in the BC-L groups. Obviously, the EMSD-L significantly accelerated wound healing by promoting wound closure and accelerating healing metabolism compared to the control (MD-L, ED-L, and BC-L) groups. These results revealed the synergistic effect of mechanical regulation and electrostimulation on accelerating wound healing in rats.

To quantify the closure rate and explore the biological mechanism under the EMSD-C intervention, the wound healing performance was further explored on circular (0.8 cm in diameter) full-thickness skin wounds (fig. S12). Similar to the treatment grouping of linear wounds, the rats were divided into four groups: EMSD-C, MD-C, ED-C, and BC-C (Fig. 5A, left). All groups were subjected to the same circular wound surgery procedure. The rats were labeled as EMSD-C_n, MD-C_n, ED-C_n, and BC-C_n (n = 1, 2, and 3), and the wound healing process was documented once every 2 days (Fig. 5A, right, and fig. S14). The series of images demonstrate that the circular wound healed much faster and formed a smaller amount of scab under an EMSD-C intervention. In contrast, the MD-C, ED-C, and BC-C groups showed delayed healing, attributed to the fact that EMSD-C accelerated the healing process from inflammation, to new tissue formation, to remodeling phase. The quantified wound closure rate over time is shown in Fig. 5B, and there was no substantial difference at day 2 for all groups. From day 4, the gap of closure rate between the EMSD-C group and control groups was gradually widening, and the closure rate of the BC-C group is much lower than those of the other three groups. The final wound closure rate

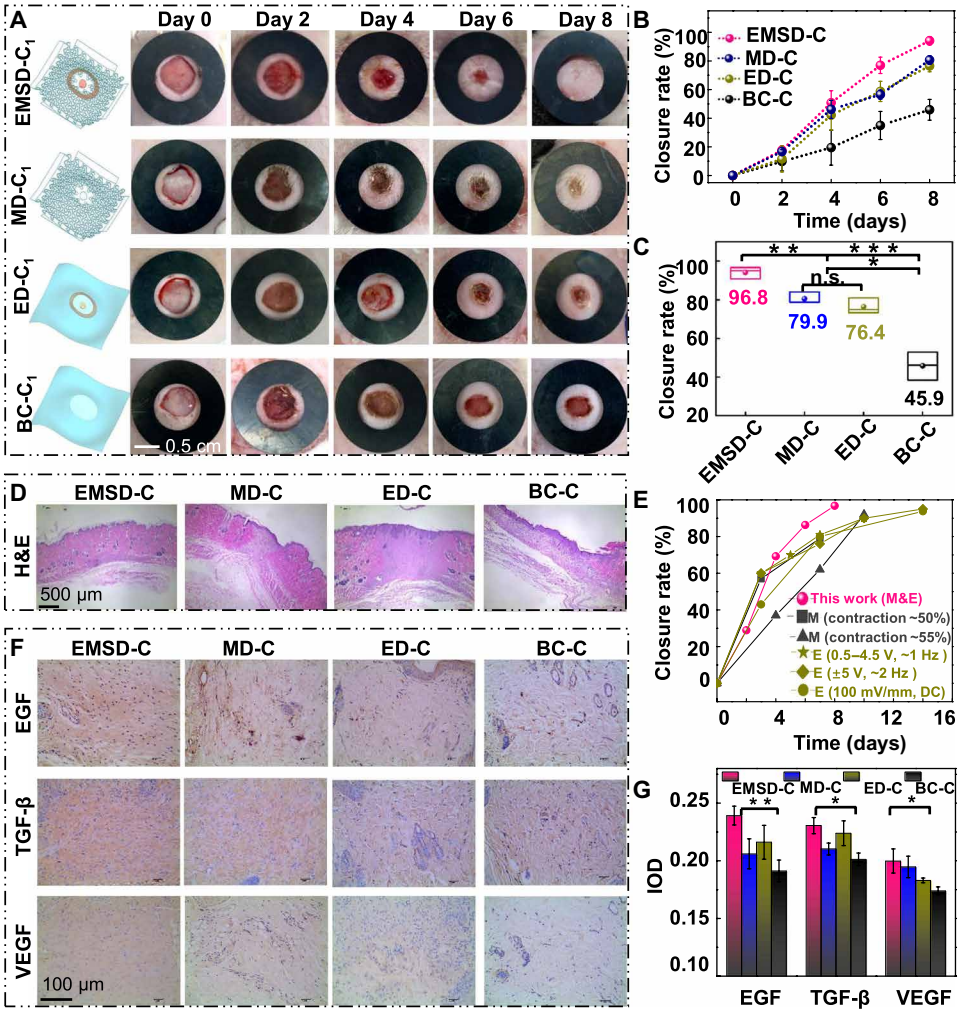

Fig. 5. Circular incisional wound healing and biological mechanism. (**A**) A series of images on the wound area over time of the EMSD-C, MD-C, ED-C, and BC-C groups (F) (n = 3). Schematics on the left show the device setup of each group. (**B**) Wound closure rate over time of the wound area from different groups. (**C**) Final wound closure rate for different groups. (**D**) H&E stains of skin at the wound site. (**E**) Wound closure rate of the EMSD-C compared to the reported results by the mechanical regulation or electric stimulation (mechanical contraction parameters, voltage, and frequency) (*48*–*52*). Mechanical regulation and electric stimulation are represented by M and E, respectively. (**F**) IHC staining images of multiple growth factors including EGF, TGF-β, and VEGF. (**G**) IHC score of the various growth factors expressed in different groups (n = 3). All data in (B) and (G) are presented as means ± SD. In box plots (C), the dot is the mean, the centerline is the median, box limits are the lower quartile (Q1) and upper quartile (Q3), and whiskers are the most extreme data points that are no more than 1.5 × (Q3 − Q1) from the box limits. n.s., not significant ($P > 0.05$); $^{**}P < 0.01$ and $^{***}P < 0.001$.

for different groups is shown in Fig. 5C. The average values measured after 8 days revealed that the closure rate of the EMSD-C group was 96.8 ± 2.9%, significantly higher than those of the control groups (79.9 ± 3% for MD-C, 76.4 ± 4% for EC-C, and 45.9 ± 7% for BC-C). The skin at the circular incisional wound site in the different groups was collected at day 8 postintervention for histological examination by H&E staining (Fig. 5D). Histological analysis revealed that the wound of the EMSD-C groups achieved reepithelialization in the center of the wounds treated with the EMSD-C, exhibiting an intact new epidermis that was tightly connected to the granulation tissue underneath. In the MD-C and ED-C groups, the connection between the new epidermis and granulation tissue was loose, indicating weaker healing than in the EMSD-C group. For comparison, the epidermis was utterly absent in the BC-C group. Our electromechanical synergistic system rapidly achieved over 96% closure rate and superb reepithelialization effect within 8 days, which obviously exceeded other reported mechanical regulation or electric stimulation approaches based on similar rat models (*48*–*52*) (Fig. 5E).

To understand the accelerated wound healing mechanism driven by the EMSD intervention, multiple growth factors related to wound healing, including EGF, TGF-β, and VEGF, were studied (*23*). At the end of day 8, skin in different groups was collected and measured by immunohistochemistry (IHC) to evaluate the distribution of these key growth factors to understand the EMSD intervention mechanism (Fig. 5F and fig. S15). IHC staining images displayed an overall expression distribution of various growth factors, which were represented by the dark brown color. In general, the IHC results showed the secretion of EGF, TGF-β, and VEGF in group EMSD-C were significantly enhanced compared to the ED-C, MD-C and BC-C groups. Finally, integrated optical density (IOD) curve analysis was conducted to quantify the expression intensity of growth factors (*29*, *53*) (Fig. 5G). The average IODs of group EMSD-C were 0.24, 0.23 and 0.20 for EGF, TGF-β, and VEGF, respectively, which were higher than those of groups MD-C (0.21, 0.21, and 0.19), ED-C (0.22, 0.22, and 0.18), and BC-C (0.19, 0.20, and 0.17). Obviously, the EGF, TGF-β, and VEGF expression of the EMSD-C group exhibited a statistically significant enhancement compared with those of the BC-C group. Moreover, the EGF expression in the MD-C and ED-C groups was higher than that of the BC-C group, suggesting that both mechanical regulation and electrostimulation can promote reepithelialization. In addition, compared with the BC-C group, the MD-C group and ED-C group can separately express higher VEGF and TGF-β, indicating that mechanical regulation and electrical stimulation play essential roles in angiogenesis and healing metabolism, respectively. These findings illustrate that the electromechanical synergistic effect had a more extraordinary ability to remodel the new epidermis and accelerate healing metabolism toward effective wound healing.

In this work, we present an electromechanical synergistic system as an effective therapeutic strategy for accelerating linear and circular wound healing. The flexible and noninvasive EMSD could render appropriate contraction by a programmable SMA metamaterial triggered by skin temperature and strengthen the endogenous electric field via a patterned antibacterial EEF. By optimizing the geometry of the EMSD, the seamlessly attachable device could provide ~10% contractile strain and a sufficient electrical field intervention at a depth of 10 mm in tissues. The wound healing performance was examined and compared among the EMSD, ED, MD, and blank groups of rats that were subjected to the wound surgery procedure and fed under the same conditions. In vivo studies demonstrated an effective wound healing in as short as 4 and 8 days for linear and circular wounds, respectively, with a statistically significant ~50% improvement in wound closure rate versus the nonintervention controls. This outstanding wound therapeutic effect surpassed most other reported nonpharmacological approaches. Furthermore, the mechanical contraction could enhance the secretion of VEGF to accelerate angiogenesis, while more TGF-β induced by electric stimulation led to the promotion of healing metabolism. Together, they synergistically promoted reepithelialization and resulted in a rapid wound repair. In general, our development provided a successful example of temperature-triggered and battery-free electromechanical synergistic intervention for biomedical applications. More broadly, it holds great promise to address personalized customization for manipulating orderly healing of irregular wounds.

MATERIALS AND METHODS

EMSD fabrication and encapsulation

The detailed fabrication process of the EMSD including a stretchable SMA metamaterial grid and a patterned EEF is depicted in fig. S1. A Ti/Ni SMA foil (~100 μm) was adhered flatly on the heat release tape, and laser cutting technology was used to prepare the SMA-L and SMA-C, respectively. These SMA grids were immersed in Ecoflex gel, taken out, and suspended to cure naturally. EEFs patterned by laser cutting technology were aligned and embedded on the Ecoflex when it was not fully cured.

Cell immunofluorescence staining

Mouse fibroblasts were cultured on the Ecoflex and reference dishes for 3 days, and they both went through the same procedure and were cultured under the same conditions. Then, the sample was first fixed with 2 to 4% formaldehyde for 15 min and rinsed with prewarmed phosphate-buffered saline (PBS) three times. The samples were then stained with Texas Red-X Phalloidin (100 nM) and Hoechst (50 nM) at 37°C for 30 min. After staining, the cells were rinsed three times with prewarmed buffer and imaged using a Nikon A1RS confocal microscope.

FEA and experimental mechanical characterization

The FEA mechanical properties of SMA grids were evaluated by the ABAQUS software. The Young's modulus and Poisson's ratio were set to 67 GPa and 0.327, and the meshes were refined to ensure computational accuracy. Then, the strain distribution of SMA grids with different stretching lengths was studied. Analysis results showed that the strain distributed at all the SMA grids with different stretching lengths are smaller than the fracture strain of 8%. A commercial mechanical machine was used to test the experimental mechanical response of the stretchable SMA metamaterial grids under different ambient temperatures (20°, 25°, 30°, 35°, 40°, 45°, and 50°C) with a loading rate of 0.02 mm/s (figs. S5 and S7).

Electric field simulation

The AMFES was used to simulate electric field distributions of the patterned antibacterial EEF. In the simulation domain, the electrostatic saltwater solution was created with the permittivity of 81 to simulate tissues and body fluids.

Antibacterial characterization

The antibacterial efficiency of the EEF was investigated by using *E. coli* (ATCC 8739) as the model bacteria. The *E. coli* stains were aerobically cultivated at 37°C to the stationary phase with Luria-Bertani medium (1% tryptone, 0.5% yeast extract, 0.5% NaCl, and 1 mM NaOH). To analyze quantitatively, the density of the bacteria was estimated by at least six fluorescence images. The absorbances of the overnight suspensions were obtained via ultraviolet-visible (UV-vis) spectroscopy at 600 nm.

Animals and diets

Six-week-old male Sprague-Dawley rats were subjected to the same linear or circular wound surgery procedure and fed under the same conditions. Briefly, all Sprague-Dawley rats were housed in separated cages in a temperature-controlled room (22°C) with a 12-hour light/12-hour dark cycle with free access to water and rodent feed. All animal experiments were performed following the standard protocol approved by the University of Electronic Science and Technology of China (1061420210617007).

Wound healing modeling and device application

The anesthesia was first induced by inhalation of 2 to 5% isoflurane and maintained with 2% isoflurane. Following anesthesia, rats were fixed in the prone position. The hair of the experiment area from the dorsal portion of all the Sprague-Dawley rats was shaved with electric hair clippers, and then the hair removal cream was evenly applied to the back. After 5 min, the back was cleaned with PBS solution. The back of the rats was scrubbed with iodine scrub and then alcohol before surgery. Two full-thickness excisional linear (1 cm) or circular (0.8 cm in diameter) skin wounds were created along the back of each rat. The EMSDs were stretched (~10%) and directly placed above the wound, and the biocompatible double-sided tape was used to fix the wound edges and device edges (fig. S12). The EMSD has the properties of easy use and painless removal, and the wound healing process was documented once every 2 days.

H&E staining of skin

Skin samples were collected from the back of rats after EMSD, ED, and MD treatment. Control skin on the back of the rat with no treatment was also collected at the same time points. Tissues were fixed with 4% formaldehyde, and slices were prepared at 3 μm for H&E staining. H&E slides were observed directly using an inverted optical microscope.

IHC properties of skin

Frozen skin samples of 10-μm thickness were fixed with cold acetone for 5 min and washed with cold PBS. IHC staining was performed to evaluate the level of VEGF, EGF, and TGF-β. The procedure of IHC of formalin-fixed paraffin-embedded skin samples was employed. Mouse anti-VEGF (NB100-664, Novus), anti-EGF, and rabbit TGF-β (NBP1-80289, Novus) were used at dilutions of 1:100, 1:100, and 1:200, respectively, as the primary antibodies, respectively.

Statistical analysis

Statistical analysis was performed by two-tailed unpaired Student's *t* tests for final wound closure rate for circular wounds. In box plots, dot is the mean, center line is the median, box limits are the lower quartile (Q1) and upper quartile (Q3), and whiskers are the most extreme data points that are no more than 1.5 × (Q3 − Q1) from the box limits. n.s., **, and *** represent nonsignificant ($P > 0.05$), $P < 0.01$, and $P < 0.001$, respectively. In general, P value less than 0.05 indicates a significant difference.

SUPPLEMENTARY MATERIALS

Supplementary material for this article is available at https://science.org/doi/10.1126/sciadv.abl8379

View/request a protocol for this paper from *Bio-protocol*.

REFERENCES AND NOTES

1. M. Kurita, T. Araoka, T. Hishida, D. D. O'Keefe, Y. Takahashi, A. Sakamoto, M. Sakurai, K. Suzuki, J. Wu, M. Yamamoto, R. H. Benitez, A. Ocampo, P. Reddy, M. N. Shokhirev, P. Magistretti, E. N. Delicado, H. Eto, K. Harii, J. C. I. Belmonte, *In vivo* reprogramming of wound-resident cells generates skin epithelial tissue. *Nature* **561**, 243–247 (2018).
2. A. J. Singer, R. A. F. Clark, Cutaneous wound healing. *N. Engl. J. Med.* **341**, 738–746 (1999).
3. T. Tahir, N. Febrianti, S. Wahyuni, Rabia, Y. Syam, Evaluation of acute wound healing potential of red dragon fruit (Hylocereus Polyrhizus) extract cream on type III collagen and epidermal growth factor (EGF) levels: An animal study. *Med. Clín. Práctica* **3**, 100091 (2020).
4. C. K. Sen, G. M. Gordillo, S. Roy, R. Kirsner, L. Lambert, T. K. Hunt, F. Gottrup, G. C. Gurtner, M. T. Longaker, Human skin wounds: A major and snowballing threat to public health and the economy. *Wound Repair Regen.* **17**, 763–771 (2009).
5. C. K. Sen, Human wounds and its burden: An updated compendium of estimates. *Adv. Wound Care* **8**, 39–48 (2019).
6. G. C. Gurtner, S. Werner, Y. Barrandon, M. T. Longaker, Wound repair and regeneration. *Nature* **453**, 314–321 (2008).
7. B. Mirani, E. Pagan, B. Currie, M. A. Siddiqui, R. Hosseinzadeh, P. Mostafalu, Y. S. Zhang, A. Ghahary, M. Akbari, An advanced multifunctional hydrogel-based dressing for wound monitoring and drug delivery. *Adv. Healthc. Mater.* **6**, 1700718 (2017).
8. S. Saghazadeh, C. Rinoldi, M. Schot, S. S. Kashaf, F. Sharifi, E. Jalilian, K. Nuutila, G. Giatsidis, P. Mostafalu, H. Derakhshandeh, K. Yue, W. Swieszkowski, A. Memic, A. Tamayol, A. Khademhosseini, Drug delivery systems and materials for wound healing applications. *Adv. Drug Deliv. Rev.* **127**, 138–166 (2018).
9. X. Wang, J. Ge, E. E. Tredget, Y. Wu, The mouse excisional wound splinting model, including applications for stem cell transplantation. *Nat. Protoc.* **8**, 302–309 (2013).
10. Y. Wu, L. Chen, P. G. Scott, E. E. Tredget, Mesenchymal stem cells enhance wound healing through differentiation and angiogenesis. *Stem Cells* **25**, 2648–2659 (2007).
11. S. L. Boxall, K. Carville, G. D. Leslie, S. J. Jansen, Treatment of anticoagulated patients with negative pressure wound therapy. *Int. Wound J.* **14**, 950–954 (2017).
12. J. Koo, M. R. MacEwan, S.-K. Kang, S. M. Won, M. Stephen, P. Gamble, Z. Xie, Y. Yan, Y.-Y. Chen, J. Shin, N. Birenbaum, S. Chung, S. B. Kim, J. K. D. V. Harburg, K. Bean, M. Paskett, J. Kim, Z. S. Zohny, S. M. Lee, R. Zhang, K. Luo, B. Ji, A. Banks, H. M. Lee, Y. Huang, W. Z. Ray, J. A. Rogers, Wireless bioresorbable electronic system enables sustained nonpharmacological neuroregenerative therapy. *Nat. Med.* **24**, 1830–1836 (2018).
13. G. Yao, L. Kang, J. Li, Y. Long, H. Wei, C. A. Ferreira, J. J. Jeffery, Y. Lin, W. Cai, X. Wang, Effective weight control via an implanted self-powered vagus nerve stimulation device. *Nat. Commun.* **9**, 5349 (2018).
14. F. B. Wagner, J. B. Mignardot, C. G. L. Goff-Mignardot, R. Demesmaeker, S. Komi, M. Capogrosso, A. Rowald, I. Seáñez, M. Caban, E. Pirondini, M. Vat, L. A. McCracken, R. Heimgartner, I. Fodor, A. Watrin, P. Seguin, E. Paoles, K. V. D. Keybus, G. Eberle, B. Schurch, E. Pralong, F. Becce, J. Prior, N. Buse, R. Buschman, E. Neufeld, N. Kuster, S. Carda, J. Zitzewitz, V. Delattre, T. Denison, H. Lambert, K. Minassian, J. Bloch, G. Courtine, Targeted neurotechnology restores walking in humans with spinal cord injury. *Nature* **563**, 65–71 (2018).
15. G. Yao, L. Kang, C. Li, S. Chen, Q. Wang, J. Yang, Y. Long, J. Li, K. Zhao, W. Xu, W. Cai, Y. Lin, X. Wang, A self-powered implantable and bioresorbable electrostimulation device for biofeedback bone fracture healing. *Proc. Natl. Acad. Sci. U.S.A.* **118**, e2100772118 (2021).
16. G. Yao, D. Jiang, J. Li, L. Kang, S. Chen, Y. Long, Y. Wang, P. Huang, Y. Lin, W. Cai, X. Wang, Self-activated electrical stimulation for effective hair Regenerationviaa wearable omnidirectional pulse generator. *ACS Nano* **13**, 12345–12356 (2019).
17. G. Yao, C. Yin, Q. Wang, T. Zhang, S. Chen, C. Lu, K. Zhao, W. Xu, T. Pan, M. Gao, Y. Lin, Flexible bioelectronics for physiological signals sensing and disease treatment. *J. Materiomics* **6**, 397–413 (2020).
18. T. Someya, Z. Bao, G. G. Malliaras, The rise of plastic bioelectronics. *Nature* **540**, 379–385 (2016).
19. S. Xu, A. Jayaraman, J. A. Rogers, Skin sensors are the future of health care. *Nature* **571**, 319–321 (2019).
20. S. Dhivya, V. V. Padma, E. Santhini, Wound dressings-A review. *Biomedicine* **5**, 22 (2015).

21. J. Li, D. J. Mooney, Designing hydrogels for controlled drug delivery. *Nat. Rev. Mater.* **1**, 16071 (2016).
22. M. Li, J. Chen, M. Shi, H. Zhang, P. X. Ma, B. Guo, Electroactive anti-oxidant polyurethane elastomers with shape memory property as non-adherent wound dressing to enhance wound healing. *Chem. Eng. J.* **375**, 121999 (2019).
23. Y. Long, H. Wei, J. Li, G. Yao, B. Yu, D. Ni, A. L. F. Gibson, X. Lan, Y. Jiang, W. Cai, X. Wang, Effective wound healing enabled by discrete alternative electric fields from wearable nanogenerators. *ACS Nano* **12**, 12533–12540 (2018).
24. P. E. Houghton, Electrical stimulation therapy to promote healing of chronic wounds: A review of reviews. *Chronic Wound Care Manage. Res.* **Volume 4**, 25–44 (2017).
25. J. D. Boerckel, B. A. Uhrig, N. J. Willett, N. Huebsch, R. E. Guldberg, Mechanical regulation of vascular growth and tissue regeneration *in vivo*. *Proc. Natl. Acad. Sci. U.S.A.* **108**, E674–E680 (2011).
26. A. Brugués, E. Anon, V. Conte, J. H. Veldhuis, M. Gupta, J. Colombelli, J. J. Muñoz, G. W. Brodland, B. Ladoux, X. Trepat, Forces driving epithelial wound healing. *Nat. Phys.* **10**, 683–690 (2014).
27. H. I. Harn, R. Ogawa, C. K. Hsu, M. W. Hughes, M. J. Tang, C. M. Chuong, The tension biology of wound healing. *Exp. Dermatol.* **28**, 464–471 (2019).
28. X. Xiao, X. Xiao, A. Nashalian, A. Libanori, Y. Fang, X. Li, J. Chen, Triboelectric nanogenerators for self-powered wound healing. *Adv. Healthc. Mater.* **14**, 2100975 (2021).
29. S. Du, N. Zhou, Y. Gao, G. Xie, H. Du, H. Jiang, L. Zhang, J. Tao, J. Zhu, Bioinspired hybrid patches with self-adhesive hydrogel and piezoelectric nanogenerator for promoting skin wound healing. *Nano Res.* **13**, 2525–2533 (2020).
30. J. Jiang, Z. Wang, L. Hao, M. Zhang, L. Cui, Z. Xia, Study on healing effect of PTFE electrets on pig wound. *IEEE 9th Intern. Sympos. Electrets* **1996**, 788–792 (1996).
31. Y. Wang, X. Sun, Q. Wang, J. Yang, P. Gong, Y. Man, J. Zhang, In vitro and in vivo evaluation of porous chitosan electret membrane for bone regeneration. *J. Bioact. Compat. Polym.* **33**, 426–438 (2018).
32. M. A. Ruehle, E. A. Eastburn, S. A. LaBelle, L. Krishnan, J. A. Weiss, J. D. Boerckel, L. B. Wood, R. E. Guldberg, N. J. Willett, Extracellular matrix compression temporally regulates microvascular angiogenesis. *Sci. Adv.* **6**, eabb6351 (2020).
33. H. Birke-Sorensen, M. Malmsjo, P. Rome, D. Hudson, E. Krug, L. Berg, A. Bruhin, C. Caravaggi, M. Chariker, M. Depoorter, C. Dowsett, R. Dunn, F. Duteille, F. Ferreira, J. M. F. Martínez, G. Grudzien, S. Ichioka, R. Ingemansson, S. Jeffery, C. Lee, S. Vig, N. Runkel, Evidence-based recommendations for negative pressure wound therapy: Treatment variables (pressure levels, wound filler and contact layer) – Steps towards an international consensus. *J. Plast. Reconstr. Aesthet. Surg.* **64**, S1–S16 (2011).
34. S. Karlakki, M. Brem, S. Giannini, V. Khanduja, J. Stannard, R. Martin, Negative pressure wound therapy for management of the surgical incision in orthopaedic surgery. *Bone Joint Res.* **2**, 276–284 (2013).
35. N. B. Morgan, Medical shape memory alloy applications—The market and its products. *Mater. Sci. Eng. A* **378**, 16–23 (2004).
36. J. M. Jani, M. Leary, A. Subic, M. A. Gibson, A review of shape memory alloy research, applications and opportunities. *Mater. Design* **56**, 1078–1113 (2014).
37. J. Liu, Y. Zhang, Soft network materials with isotropic negative Poisson's ratios over large strains. *Soft Matter* **14**, 693–703 (2018).
38. H. Zhang, X. Guo, J. Wu, D. Fang, Y. Zhang, Soft mechanical metamaterials with unusual swelling behavior and tunable stress-strain curves. *Sci. Adv.* **4**, eaar8535 (2018).
39. C. Wang, S. Zou, W. Zhao, Y. Wang, G. Zhou, Multi-objective explosion-proof performance optimization of a novel vehicle door with negative Poisson's ratio structure. *Struct. Multidisp. Optim.* **58**, 1805–1822 (2018).
40. J. Huang, Q. Zhang, F. Scarpa, Y. Liu, J. Leng, In-plane elasticity of a novel auxetic honeycomb design. *Compos. B Eng.* **110**, 72–82 (2017).
41. K.-I. Jang, H. U. Chung, S. Xu, C. H. Lee, H. Luan, J. Jeong, H. Cheng, G.-T. Kim, S. Y. Han, J. W. Lee, J. Kim, M. Cho, F. Miao, Y. Yang, H. N. Jung, M. Flavin, H. Liu, G. W. Kong, K. J. Yu, S. I. Rhee, J. Chung, B. Kim, J. W. Kwak, M. H. Yun, J. Y. Kim, Y. M. Song, U. Paik, Y. Zhang, Y. Huang, J. A. Rogers, Soft network composite materials with deterministic and bio-inspired designs. *Nat. Commun.* **6**, 6566 (2015).
42. M. Es-Souni, M. Es-Souni, H. F. Brandies, On the transformation behaviour, mechanical properties and biocompatibility of two NiTi-based shape memory alloys: $NiTi_{42}$ and $NiTi_{42}Cu_7$. *Biomaterials* **22**, 2153–2161 (2001).
43. M. Iijima, H. Ohno, I. Kawashima, K. Endo, I. Mizoguchi, Mechanical behavior at different temperatures and stresses for superelastic nickel-titanium orthodontic wires having different transformation temperatures. *Dent. Mater.* **18**, 88–93 (2002).
44. M. Zhao, B. Song, J. Pu, T. Wada, B. Reid, G. Tai, F. Wang, A. Guo, P. Walczysko, Y. Gu, T. Sasaki, A. Suzuki, J. V. Forrester, H. R. Bourne, P. N. Devreotes, C. D. McCaig, J. M. Penninger, Electrical signals control wound healing through phosphatidylinositol-3-OH kinase-γ and PTEN. *Nature* **442**, 457–460 (2006).
45. B. Song, Y. Gu, J. Pu, B. Reid, Z. Zhao, M. Zhao, Application of direct current electric fields to cells and tissues *in vitro* and modulation of wound electric field *in vivo*. *Nat. Protoc.* **2**, 1479–1489 (2007).
46. F. Gao, X. Li, T. Zhang, A. Ghosal, G. Zhang, H. M. Fan, L. Zhao, Iron nanoparticles augmented chemodynamic effect by alternative magnetic field for wound disinfection and healing. *J. Control. Release* **324**, 598–609 (2020).
47. Y. Yang, L. Ma, C. Cheng, Y. Deng, J. Huang, X. Fan, C. Nie, W. Zhao, C. Zhao, Nonchemotherapic and robust dual-responsive nanoagents with on-demand bacterial trapping, ablation, and release for efficient wound disinfection. *Adv. Funct. Mater.* **28**, 1705708 (2018).
48. J. Hu, T. Wei, H. Zhao, M. Chen, Y. Tan, Z. Ji, Q. Jin, J. Shen, Y. Han, N. Yang, L. Chen, Z. Xiao, H. Zhang, Z. Liu, Q. Chen, Mechanically active adhesive and immune regulative dressings for wound closure. *Matter* **4**, 2985–3000 (2021).
49. S. O. Blacklow, J. Li, B. R. Freedman, M. Zeidi, C. Chen, D. J. Mooney, Bioinspired mechanically active adhesive dressings to accelerate wound closure. *Sci. Adv.* **5**, eaaw3963 (2019).
50. S. Du, N. Zhou, G. Xie, Y. Chen, H. Suo, J. Xu, J. Tao, L. Zhang, J. Zhu, Surface-engineered triboelectric nanogenerator patches with drug loading and electrical stimulation capabilities: Toward promoting infected wounds healing. *Nano Energy* **85**, 106004 (2021).
51. S. H. Jeong, Y. Lee, M. G. Lee, W. J. Song, J. U. Park, J. Y. Sun, Accelerated wound healing with an ionic patch assisted by a triboelectric nanogenerator. *Nano Energy* **79**, 105463 (2021).
52. L. Mao, S. Hu, Y. Gao, L. Wang, W. Zhao, L. Fu, H. Cheng, L. Xia, S. Xie, W. Ye, Z. Sui, G. Yang, Biodegradable and electroactive regenerated bacterial cellulose/MXene ($Ti_3C_2T_x$) composite hydrogel as wound dressing for accelerating skin wound healing under electrical stimulation. *Adv. Healthc. Mater.* **9**, 2000872 (2020).
53. N. Qipshidze, N. Metreveli, P. K. Mishra, D. Lominadze, S. C. Tyagi, Hydrogen sulfide mitigates cardiac remodeling during myocardial infarction via improvement of angiogenesis. *Int. J. Biol. Sci.* **8**, 430–441 (2012).

Acknowledgments: This work was supported by the National Natural Science Foundation of China under grant numbers 61825102, 62001096, 61901085, and 52021001; Science and Technology Department of Sichuan Province under grant no. 2021YJ0362; and the Fundamental Research Funds for the Central Universities, UESTC under grant nos. ZYGX2020ZB041, ZYGX2021YGLH002, and ZYGX2021YGLH007. **Author contributions:** G.Y. conceived the concept. Y.L. and L.H. provided laboratory assistance. G.Y. and Y.L. supervised the project. G.Y., X.M., C.Y., W.L., S.H., and Q.W. designed the device, performed the experiments, and generated data in all figures. S.C., L.M., T.P., and K.Z. participated in experiments and analysis for voltage signals. G.Y. and Y.L. analyzed the data and wrote the manuscript. All authors reviewed and commented on the manuscript. **Competing interests:** The authors declare that they have no competing interests. **Data and materials availability:** All data needed to evaluate the conclusions in the paper are present in the paper and/or the Supplementary Materials.

Submitted 24 August 2021
Accepted 3 December 2021
Published 26 January 2022
10.1126/sciadv.abl8379